

---

# Pre-main sequence accretion of low-mass stars in the Cesam2k20 code

---

Student  
Ducheng Lu

Supervisors  
Dr. Ludovic Petitedemange  
Dr. João Pedro Cadilhe Marques  
Dr. Louis Manchon  
Dr. Charly Pinçon

June 2025

# Contents

<b>1</b>	<b>Introduction</b>	<b>1</b>
<b>2</b>	<b>Pre-main sequence accretion</b>	<b>2</b>
2.1	Pre-main sequence magnetospheric accretion . . . . .	2
2.2	Observational evidence of magnetospheric accretion . . .	4
<b>3</b>	<b>Stellar evolution modeling</b>	<b>4</b>
3.1	Stellar structure equations . . . . .	4
3.2	Pre-main sequence evolution . . . . .	6
3.2.1	Pre-main sequence evolution with constant mass .	6
3.2.2	Pre-main sequence evolution with accretion . . . .	8
<b>4</b>	<b>Methods</b>	<b>9</b>
4.1	Modeling the consequences of accretion . . . . .	9
4.1.1	Gravitational energy . . . . .	9
4.1.2	Deuterium burning . . . . .	10
4.1.3	Hot and cold accretion . . . . .	10
4.2	The stellar evolution code Cesam2k20 . . . . .	10
4.2.1	Lagrangian variables . . . . .	10
4.2.2	Automatic location of grid points . . . . .	10
4.2.3	Structure equations . . . . .	11
4.2.4	Input physics . . . . .	12
4.2.5	PMS initial models . . . . .	12
4.3	Accretion in Cesam2k20 . . . . .	13
4.3.1	From Lagrangian to Homologous variables . . . .	13
4.3.2	Modifications to the structure equations . . . . .	14
4.3.3	Limiting the maximum change in gravitational en- ergy . . . . .	14
4.3.4	Limiting the maximum change in mass . . . . .	14
<b>5</b>	<b>Results</b>	<b>14</b>
5.1	The toy problem . . . . .	14
5.2	The effect of different initial models . . . . .	14
5.3	The effect of different accretion rates . . . . .	14
5.4	The effect of different chemical compositions . . . . .	14
5.5	Comparison with Palla & Stahler (1993) . . . . .	14
<b>6</b>	<b>Conclusion</b>	<b>16</b>
	<b>References</b>	<b>17</b>



**Abstract**

*Context.*

*Aim.*

*Methods.*

*Results.*

**Abstract**

*Contexte.*

*Objectif.*

*Méthodes.*

*Résultats.*

# 1 Introduction

Stars form through the gravitational collapse of dense regions within molecular clouds. When the self-gravity of such a region overcomes the opposing pressure and magnetic support, collapse begins. This process is typically nonhomologous, with the central regions collapsing more rapidly than the outer ones.

Initially, the collapse is isothermal, as radiation efficiently maintains the thermal equilibrium of the system. As the density increases, the central region becomes increasingly opaque to radiation, inhibiting its escape from the core while still allowing it from the outer layers. This growing opacity leads to an adiabatic collapse of the center, during which the temperature and pressure rise until a hydrostatic core, or a protostar, is formed (e.g., Stahler and Palla 2004). The protostar then accretes material from the surrounding cloud, a process that can continue for several million years.

Once most of the surrounding material has been accreted, the protostar enters the pre-main sequence (PMS) phase and becomes visible as a T Tauri star (TTS). TTSs are cold PMS stars that serve as precursors to low-mass main-sequence stars of spectral types F, G, K, and M. Classical T Tauri stars (CTTSs) are characterized by strong infrared (IR) emission from their optically thick accretion disks. As accretion declines due to the depletion of material in the inner disk, the IR emission weakens, and the stars are then observed as weak T Tauri stars (WTTSs). Similarly, young massive stars are also expected to undergo accretion during their early evolution and are observed as Herbig Ae/Be stars—hotter and more luminous than TTSs. However, the accretion processes for these higher-mass stars remain poorly understood.

The earliest accretion stages remain observationally elusive, as protostars are deeply embedded in the surrounding dusty cloud, making it highly extincted in optical and near-IR wavelengths. Nonetheless, indirect indicators such as disks, outflows, and jets provide compelling evidence of ongoing accretion. Modeling these stages remains challenging due to the time-variable, non-linear nature of the process and the complexity of the underlying physics.

When Henyey et al. (1955) and Hayashi (1961) first studied the early phases of stellar evolution, accretion was not taken into account. Instead, stars were assumed to begin their evolution as fully convective objects with very large radii and luminosities, contracting under their own gravity until a radiative core developed, eventually reaching the main sequence. These evolutionary paths are now known as the Hayashi and Henyey tracks. Since Larson (1969) introduced the concept of the formation of a hydrostatic core, followed by continued accretion from an infalling envelope of gas and dust, accretion has been recognized as a fundamental process in early stellar evolution, supported by both theoretical and observational studies.

There has been growing interest in studying accretion in PMS stars since the discovery of exoplanetary systems, particularly because of its relevance to planetary formation. Accretion disks are the birthplaces of planets and other small bodies, making the study of accretion crucial for understanding the early evolution of planetary systems. Beyond this, accretion can significantly influence the internal structure and rotation of stars by supplying both mass and angular momentum. In particular, accretion sets the initial distribution of angular momentum, which influences the star's rotational evolution and internal dynamics. These structural and rotational changes can, in turn, affect the stellar dynamo mechanism responsible for amplifying magnetic fields in young stars (e.g., Stelzer and Neuhauser 2001).

Accretion also impacts long-term stellar evolution by setting the initial conditions for subsequent evolutionary stages and can leave lasting imprints. Consequently, it can di-

rectly affect the determination of fundamental stellar parameters such as age, mass, and radius, which are crucial not only for stellar physics but also for fields like exoplanet characterization and galactic archaeology. In addition, accretion can alter the surface chemical composition, especially if the accreted material differs in abundance from that of the protostar (Kunitomo and Guillot 2021). This has important implications for interpreting observed stellar abundances and for modeling chemical mixing processes.

Finally, accretion history plays a critical role in understanding young stellar clusters. It can influence the shape of the initial mass function, contribute to the observed luminosity spread among cluster members, and affect the positioning of stars on theoretical isochrones (Baraffe et al. 2009, 2012; Hosokawa et al. 2011). Accurate modeling of accretion is therefore important for interpreting observed features of young clusters.

In this project, I investigate the impact of accretion on stellar structure and evolution using the Cesam2k20 version of the 1D stellar evolution code *Code d'Évolution Stellaire Adaptatif et Modulaire* (CESAM) (Marques et al. 2013; Morel 1997; Morel and Lebreton 2008). Our goal is to implement accretion in Cesam2k20, which will allow us to examine its effects on stellar evolution and structure, and to compare the results with theoretical predictions and other stellar evolution models.

This study focuses on the later stages of the accretion process, after the formation of a hydrostatic core. We restrict our analysis to low-mass stars, as accretion in high-mass stars remains less constrained and falls outside the scope of this work.

A parallel branch of the original CESAM code, *Code d'Évolution Planétaire Adaptatif et Modulaire* (CEPAM) (Guillot and Morel 1995), has been developed for modeling planetary formation and evolution. A future unification of these two branches would provide a powerful framework for studying the coupled evolution of stars and their planetary systems.

In the next section, I review the current understanding of pre-main sequence accretion, including the mechanisms of magnetospheric accretion and a brief overview of the observational evidence supporting it. Sec.3 presents the fundamental equations governing stellar structure and outlines how pre-main sequence evolution is modeled in stellar evolution codes. In Sec.4, I begin by discussing the modeling of the consequences of accretion, followed by a description of the Cesam2k20 code, including its numerical structure and input physics. I then detail the implementation of accretion in the code. The results of my models are presented in Sec.5, where I explore the effects of different accretion rates and deuterium abundances, and compare our findings with previous work by Palla and Stahler (1993). Finally, Sec.6 summarizes our main findings, discusses the limitations of the current work, and outlines future prospects.

## 2 Pre-main sequence accretion

In this section, I will review the current understanding of stellar accretion, including the mechanisms of magnetospheric accretion and the observational evidence for accretion in pre-main sequence stars.

### 2.1 Pre-main sequence magnetospheric accretion

Stellar magnetic fields play a crucial role in the accretion of pre-main sequence stars, through the mechanism known as magnetospheric accretion (See, for example, Hartmann et al. 2016, for a review). Fig. 1 is a schematic illustration of magnetospheric accretion onto young ( $1 \lesssim t \lesssim 10$ , Myr), low-mass ( $\lesssim 1M_{\odot}$ ) stars. The strong stellar magnetic

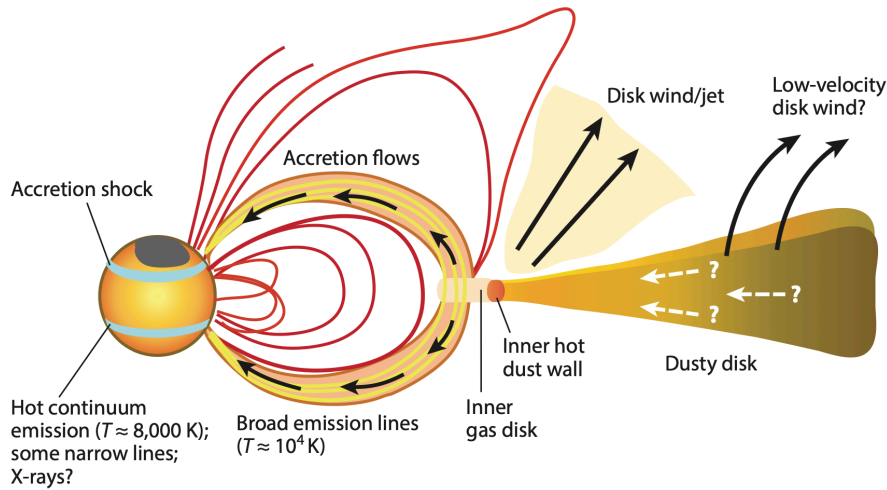


Figure 1: Schematic illustration of magnetospheric accretion onto young low-mass stars. The strong stellar magnetic field truncates the circumstellar disk at a few stellar radii. Accreting material is channeled along the magnetic field lines and impacts the stellar surface, forming an accretion shock. Jets and disk winds may also play a role in the star-disk interaction. The exact mechanisms for mass and angular momentum transport in the star-disk system remain uncertain. The figure is reproduced from Fig. 1 of Hartmann et al. (2016).

field truncates the circumstellar disk at a few stellar radii. The dust disk is truncated slightly farther out than the gas disk, as dust in the inner disk sublimates due to heating by the stellar radiation field. The inner edge of the dust disk is responsible for most of the observed near-IR excess. Material from the disk is funneled onto the star along the magnetic field lines, where it is heated to approximately  $10^4$  K, producing broad emission lines. The accretion flow is accelerated along the field lines, eventually reaching the stellar surface at nearly free-fall velocity. This process leads to the formation of an accretion shock at the stellar surface, where the gas is briefly halted and heated to very high temperatures, emitting X-rays. Most of these X-rays are absorbed and reradiated in the ultraviolet and optical continuum.

Despite recent advances in the study of magnetospheric accretion, many aspects are still under debate. Bouvier (2014) summarizes several open issues regarding the physics of the magnetospheric accretion and ejection processes. One of the long-standing problems is the evolution of stellar rotation: while the angular momentum carried by accreting material should spin up the star, observations reveal that the rotation rates of PMS stars are lower than expected. This discrepancy suggests that some form of magnetic braking must be at work to regulate stellar spin (e.g., Herbst et al. 2007).

Magnetohydrodynamic simulations suggest that jets, disk winds, and magnetospheric ejections are involved in removing angular momentum during accretion (e.g., Ireland et al. 2020; Lii et al. 2014; Romanova et al. 2004). However, the relative importance of these mechanisms in shaping the angular momentum evolution remains under investigation (e.g., Kunitomo et al. 2017). Although the models presented in this work do not include magnetic fields or rotation, understanding the broader framework of magnetospheric accretion is essential for interpreting how accretion affects stellar structure. Including these physical processes for more realistic accretion modeling will be an important direction for future work.

## 2.2 Observational evidence of magnetospheric accretion

Observations of CTTs provide strong evidence for magnetospheric accretion, including the presence of strong stellar magnetic fields, an inner cavity of a few stellar radii within the magnetosphere, magnetic accretion columns filled with free-falling plasma, and accretion shocks at the stellar surface.

The accretion shock produces emission in the ultraviolet, optical, and near-infrared wavelengths, as well as a modest amount of X-rays. These emissions serve as crucial diagnostics of the accretion region, allowing measurements of the accretion luminosity which, when combined with stellar mass and radius, provide estimates of accretion rates. Soft X-ray emission, unique to accreting stars, has also been detected from CTTs and is likely produced in the post-shock region (e.g., Kastner et al. 2002). Magnetospheric accretion flows can be identified by redshifted absorption features in specific spectral lines (Muzerolle et al. 2001), while blueshifted forbidden emission lines have been linked to strong winds and mass outflows (e.g., Bally 2016).

Magnetospheric accretion paradigm assumes that the stellar magnetic field is strong enough to counteract the pressure of the accretion disk and disrupt the disk before it reaches the stellar surface (e.g., Koenigl 1991). At the truncation radius  $R_{\text{trunc}}$ , the magnetic pressure approximately balances the gas ram pressure, i.e.,  $B^2/8\pi \simeq \frac{1}{2}\rho v^2$ , where the relevant velocity is roughly the Keplerian velocity,  $v = \sqrt{GM_\star/R_{\text{trunc}}}$ . The exact location of this truncation radius will also depend on the accretion rate (see Eq. 2.2 in Bouvier et al. 2007). This framework generally aligns with the measured magnetic field strengths of CTTs, which typically range from a few hundred Gauss to a few kiloGauss (Alencar et al. 2012; Bouvier et al. 2007).

## 3 Stellar evolution modeling

Stellar evolution modeling involves combining physical principles with numerical methods to simulate how stars change over time. This section first introduces the fundamental equations that describe stellar evolution and then turns the focus to the modeling of pre-main sequence stars.

### 3.1 Stellar structure equations

Modeling stellar evolution involves defining initial conditions and solving the differential equations that govern the physical processes inside a star, thereby predicting how stellar properties change over time. The primary factors determining an isolated star's evolution are its mass and initial chemical composition. Once specified, these initial parameters are input into the stellar structure equations, which express the physical quantities as functions of position and time  $(\vec{r}, t)$ . By assuming spherical symmetry, the position can be reduced to the radial distance  $r$  from the center, so physical quantities become functions of radius and time, i.e.,  $(r, t)$ .

Throughout most of stellar evolution, the total stellar mass remains nearly constant except in cases of significant mass loss. In contrast, the stellar radius can vary rapidly as the star passes through different stages. Because Lagrangian coordinates move with the fluid elements, it is more convenient to use the mass coordinate  $m$ , defined as the total mass enclosed within radius  $r$ , rather than the radius itself. This approach allows us to track the evolution of specific mass shells as they move and change, making it a more natural choice for describing properties such as energy production, chemical composition and angular momentum within the stellar interior.



In the mass coordinate, the system of 1D stellar structure equations can be written as (See, for example, Kippenhahn et al. 2013):

$$\frac{\partial p}{\partial m} = -\frac{Gm}{4\pi r^2}, \quad (1a)$$

$$\frac{\partial T}{\partial m} = \frac{\partial p}{\partial m} \frac{T}{p} \nabla, \quad (1b)$$

$$\frac{\partial r}{\partial m} = \frac{1}{4\pi r^2 \rho}, \quad (1c)$$

$$\frac{\partial l}{\partial m} = \epsilon_{\text{nuc}} - \epsilon_{\nu} + \epsilon_{\text{g}}, \quad (1d)$$

$$\frac{\partial X_i}{\partial t} = -\frac{\partial F_i}{\partial m} + \Psi_i(P, T, \mathbf{X}), 1 \leq i \leq n_{\text{elem}}, \quad (1e)$$

where  $G$  is the gravitational constant,  $\nabla \equiv \partial \ln T / \partial \ln p$  is the temperature gradient, and  $\epsilon_{\text{nuc}}$ ,  $\epsilon_{\nu}$ , and  $\epsilon_{\text{g}}$  are the rates of nuclear energy production, neutrino energy loss, and gravitational energy production, respectively, all expressed in units of power per unit mass.  $X_i$  is the abundance of the chemical element  $i$ ,  $F_i$  is the flux of the chemical element  $i$  due to diffusion,  $\mathbf{X} \equiv \{X_i\}$  is the chemical composition vector,  $\Psi_i$  is the rate of change of  $X_i$  by thermonuclear reactions, and  $n_{\text{elem}}$  is the total number of chemical species considered. All quantities ( $p, l, \rho, T, \epsilon, \epsilon_{\nu}$ , etc.) are evaluated locally at each stellar layer.

Eq. (1a) describes the hydrostatic equilibrium and Eq. (1c) describes the mass continuity. Eq. (1d) and Eq. (1b) describe the energy production and energy transport, respectively. These equations illustrate a close coupling between stellar structure and the process of energy production and transport. In most stars, energy is primarily transported by radiation and convection, and the value of  $\nabla$  depends on the dominant mechanism of energy transport. Eq. (1e) describes the evolution of the chemical composition of the star, which is governed by the nuclear reactions occurring in the star and the transport of chemical elements. This set of equations assumes spherical symmetry and does not account for magnetic fields nor rotation. These are common simplifications in 1D stellar models and are sufficient for many evolutionary studies.

Stellar evolution is typically treated as a one-dimensional boundary value problem with initial conditions given by the initial mass and chemical composition of the star. The boundary conditions are set at the center and surface of the star. Spherical symmetry requires that the radius, luminosity, and chemical element fluxes vanish at the center of the star. Therefore, it is imposed that:

$$r(0, t) = 0, l(0, t) = 0, F_i(0, t) = 0, i = 1, \dots, n_{\text{elem}}. \quad (2)$$

At the surface, the pressure and temperature are set to the values at the base of the stellar atmosphere:

$$p(M_{\star}, t) = p_{\text{atm}}(L_{\star}, R_{\star}, t), T(M_{\star}, t) = T_{\text{atm}}(L_{\star}, R_{\star}, t), \quad (3)$$

where  $M_{\star}$ ,  $L_{\star}$ , and  $R_{\star}$  are the stellar mass, luminosity, and radius, respectively. The values of  $p_{\text{atm}}$  and  $T_{\text{atm}}$  are derived from reconstruction of the stellar atmosphere, which typically uses empirical relations. As this project focuses on internal structure, I will not delve into the specifics of atmospheric modeling.

With both central and surface boundary conditions specified, and the evolution equations defined in Lagrangian coordinates, the stellar structure problem becomes a well-posed initial-boundary value problem. This framework serves as the basis for numerical

stellar evolution codes, which solve these equations to track the stellar evolution over time.

The solutions to the stellar structure equations yield key observable properties of stars, most notably their luminosity  $L$  and effective surface temperature  $T_{\text{eff}}$ . These two parameters define a star’s position on the Hertzsprung-Russell (HR) diagram, a fundamental tool in astrophysics to understand and visualize stellar evolution. The HR diagram helps to reveal distinct evolutionary stages such as the pre-main sequence, main sequence, and giant branch, offering a simple way to compare models with observations.

However, translating the underlying physics into stellar models is a complex task. In practice, stellar evolution codes can differ substantially in their model initialization methods. These differences can lead to notable variations during the early evolutionary stages, which will be discussed in the Sec. 3.2. Furthermore, differences in formulations, assumptions, and adopted physical ingredients, such as the equation of state (EoS) and opacities, can substantially influence the predicted stellar properties, often resulting in discrepancies between models. Therefore, it is essential to carefully consider the specific implementations and assumptions of each code when interpreting stellar evolution results. One of the goals of this project is to benchmark our accretion models against those implemented in other stellar evolution codes. The details of our physical inputs will be discussed in Sec. 4.2.

## 3.2 Pre-main sequence evolution

### 3.2.1 Pre-main sequence evolution with constant mass

Classically, the modeling of PMS evolution begins with a fully convective star of large radius and luminosity. As the star contracts under gravity, the release of gravitational energy heats the stellar interior. This contraction continues until the central temperature becomes high enough to slow down the contraction and trigger the formation of a radiative core.

The initial phase of PMS evolution is characterized by a rapid decrease in both radius and luminosity, while the effective temperature remains nearly constant. This phase, known as the Hayashi track (Hayashi 1961), defines the locus in the HR diagram of fully convective stars of a given mass and composition. Energy transport is dominated by convection during this phase. The precise location and slope of the Hayashi track is also sensitive to the treatment of convection, typically modeled using the mixing-length theory (Cox and Giuli 1968). As the star contracts, its density increases, which in turn increases the opacity of the stellar material. The resulting decrease in radiative efficiency causes a reduction in luminosity. The Hayashi tracks appear on the far right of the HR diagram and follow a steep, nearly vertical path.

The Hayashi track terminates at a minimum luminosity, where the central temperature becomes high enough for hydrogen to be fully ionized. This leads to a substantial drop in opacity in the central regions, making radiative transport more efficient, and a radiative core forms. The star then evolves toward higher effective temperatures while its luminosity remains approximately constant. This marks the beginning of the second phase of PMS evolution, where the star follows a more horizontal path in the HR diagram, known as the Henyey track, first described by Henyey et al. (1955). During this stage, the star evolves with a radiative core while maintaining a convective envelope.

This classic two-phase PMS evolution—first descending the vertical Hayashi track, then moving leftwards on the more horizontal Henyey track—is illustrated in Fig. 2, which shows evolutionary tracks for Cesam2k20 models with masses between 1 and

5,  $M_{\odot}$ , assuming initial composition  $X \simeq 0.73$ ,  $Y \simeq 0.25$  (see Sec.4.2 for details of the input physics). Arrows indicate the direction of stellar evolution, with mass labels marking the ends of each track. The nearly vertical portion corresponds to fully convective contraction (Hayashi track), while the more horizontal portion marks the emergence of a radiative core (Heney track)..

During PMS evolution, gravitational contraction remains the primary energy source, as the central temperature has not yet reached the threshold for hydrogen fusion. However, light elements such as deuterium and lithium can be burned at relatively low temperatures (Kippenhahn et al. 2013).

Deuterium burning is particularly important in PMS evolution, proceeding via the reaction:

$$^2\text{H} + ^1\text{H} \rightarrow ^3\text{He} + \gamma, \quad \Delta E_{\text{D}} = 5.5 \text{ MeV}, \quad (4)$$

which ignites at central temperature of  $T_c \sim 10^6$ , K.

Lithium burning, involving the dominant isotope  $^7\text{Li}$ , occurs via the reaction:

$$^7\text{Li} + ^1\text{H} \rightarrow ^4\text{He} + ^4\text{He} + \gamma, \quad \Delta E_{\text{Li}} = 17.6 \text{ MeV}, \quad (5)$$

which sets in at  $T_c \sim 2.5 \times 10^6$ , K. Although lithium burning releases significantly more energy per reaction than deuterium burning, the former makes little contribution to the total energy production in PMS stars, as lithium is around  $10^3$  less abundant than deuterium (Grevesse and Sauval 1998).

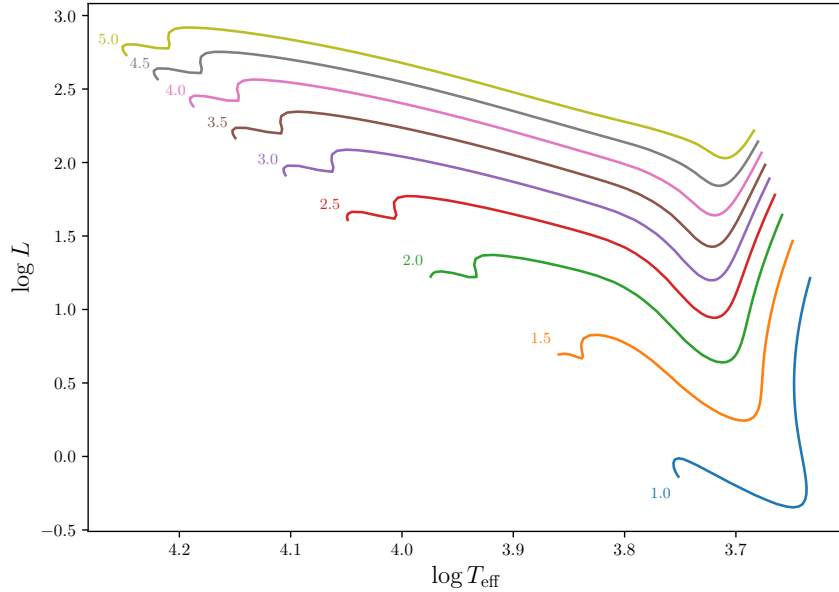


Figure 2: Classic pre-main sequence evolutionary tracks for Cesam2k20 models with masses between 1 and 5,  $M_{\odot}$  in the HR diagram. Arrows indicate the direction of stellar evolution, with stellar masses in solar masses labeled at the end of each track. The nearly vertical Hayashi track corresponds to fully convective contraction, while the more horizontal Heney track marks the phase when contraction slows down and a radiative core develops.

The star is considered to have reached the main sequence once hydrogen fusion becomes the dominant source of energy production, at a central temperature of  $T_c \sim 10^7$  K. This beginning of main sequence evolution is referred to as the Zero-Age Main Sequence (ZAMS). From the ZAMS onward, the star's position in the HR diagram changes relatively slowly during the long phase of central hydrogen burning.

### 3.2.2 Pre-main sequence evolution with accretion

The classic PMS evolution described above assumes that the star has already acquired its final mass at the beginning of contraction. However, as the observational evidence discussed in Sec. 2.2 indicates, many young stars continue to accrete material from their surrounding environment during the PMS phase. These stars experience a period of relaxation and thermal re-adjustment as they contract, before eventually settling onto a track that closely follows the constant-mass evolution (Kippenhahn et al. 2013).

One physical quantity of importance in this context is the mass accretion rate  $\dot{M}_{\text{acc}}$ , defined as the rate at which mass is transferred from the surrounding cloud to the proto-star. Estimates of  $\dot{M}_{\text{acc}}$  are often uncertain by factors of a few, due to their sensitivity to stellar parameters and extinction. These values are typically calculated from the accretion luminosity  $L_{\text{acc}}$  via:

$$L_{\text{acc}} = \frac{GM_{\star}\dot{M}_{\text{acc}}}{R_{\star}} \left(1 - \frac{R_{\star}}{R_{\text{trunc}}}\right), \quad (6)$$

assuming the material falls freely from the truncation radius  $R_{\text{trunc}}$  to the stellar surface at radius  $R_{\star}$ , (see review by Hartmann et al. 2016).

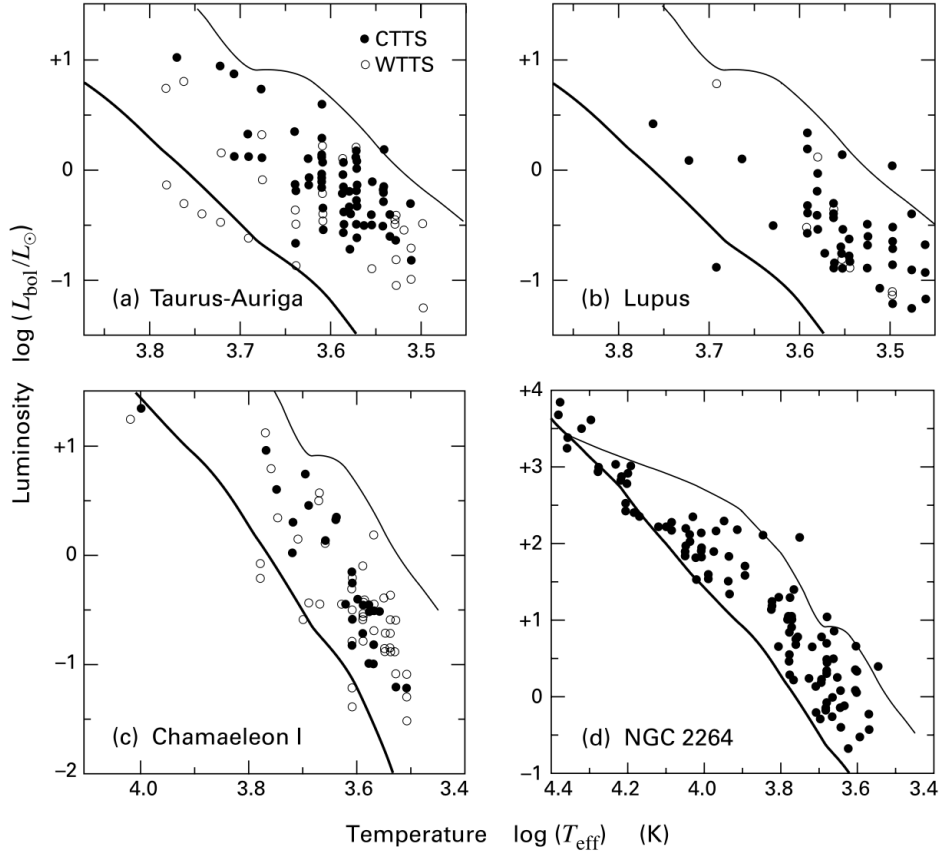


Figure 3: HR diagrams for four stellar associations. In panels (a)-(c), closed circles represent CTTSs, while open circles are WTTs. In panel (d), the sample includes CTTSs, Herbig Ae/Be stars, and main sequence objects. The thin upper curves are the theoretical birthlines; the thick lower curves are the ZAMS. Reproduced from Fig. 4.9 of Stahler and Palla (2004).

Observational studies reveal a correlation between accretion rates and stellar mass, with more massive stars accreting at higher rates (e.g., Lanzafame et al. 2023; Manara et al. 2017; Muzerolle et al. 2003; Rugel et al. 2018). Models of viscous disk evolution

predict a declining  $\dot{M}_{\text{acc}}$  with stellar age as the circumstellar disk becomes depleted (e.g., Gorti and Hollenbach 2009; Hartmann et al. 1998). Despite this, the precise functional form of the mass and time dependence remains under debate. For this study, a constant accretion rate  $\dot{M}_{\text{acc}}$  is adopted for simplicity.

Deuterium plays a more prominent role in accreting PMS stars than in non-accreting ones, as the accretion flow continuously supplies fresh deuterium. In contrast, non-accreting stars can deplete their initial deuterium rapidly. This deuterium contributes to energy generation through nuclear burning at a rate given by

$$\epsilon_D = [\text{D}/\text{H}] \epsilon_{D,0} \left( \frac{\rho}{1, \text{g cm}^{-3}} \right) \left( -\frac{T}{1 \times 10^6, \text{K}} \right)^{n_D}, \quad (7)$$

where  $\epsilon_{D,0} = 4.19 \times 10^7, \text{erg g}^{-1}, \text{s}^{-1}$ ,  $n_D = 11.8$ , and  $[\text{D}/\text{H}]$  is the number density of deuterium relative to hydrogen in the environment (cf. Eq. 11.27 in Stahler and Palla 2004).

The amount of deuterium in the accreted material can strongly influence PMS evolution. High deuterium abundance leads to significant stellar expansion during accretion, while low abundance results in a smaller size of the star throughout evolution toward the main sequence (Kunitomo et al. 2017).

When the main accretion phase ends, the circumstellar disk has mostly been dissipated and become optically thin, allowing the star to appear as a visible object. The locus in the HR diagram where PMS stars of different masses first become visible is known as the birthline (Stahler 1983). Its position is sensitive to the star's accretion history, initial mass, and chemical composition.

Theoretical birthlines can be compared with observations of TTSS to evaluate models of PMS evolution. Moreover, the birthline provides insights into the environments in which stars are formed. In Fig. 3, observations of four stellar associations with active star formation are plotted alongside the theoretical birthline and the ZAMS. Stars located below the birthline have recently dispersed their circumstellar envelopes, whereas younger, still-embedded stars cannot yet be placed on the HR diagram due to difficulties in measuring their effective temperatures.

## 4 Methods

### 4.1 Modeling the consequences of accretion

As discussed in Sec. 2.1, accretion is a highly complex process with many physical mechanisms at play. In the context of stellar evolution, some simplifications are necessary to make the problem tractable. In this section, we discuss how to model the consequences of accretion on stellar structure and evolution, including the treatment of gravitational energy, deuterium burning, and the distinction between hot and cold accretion.

#### 4.1.1 Gravitational energy

In a chemically homogeneous star, the Kippenhahn approximation can be used to calculate the energy product rate due gravitational contraction and expansion:

$$\epsilon_g = -T \frac{ds}{dt}, \quad T \frac{ds}{dt} \xrightarrow{\text{Kipp}} c_p \frac{\partial T}{\partial t} - \frac{\delta}{\rho} \frac{\partial P}{\partial t}. \quad (8)$$

As PMS stars are usually fully convective, the Kippenhahn approximation is applicable.

### 4.1.2 Deuterium burning

- equations for deuterium burning
- formula for the estimation of luminosity due to deuterium burning

### 4.1.3 Hot and cold accretion

## 4.2 The stellar evolution code Cesam2k20

We use the stellar evolution code Cesam2k20 (Marques et al. 2013; Morel 1997; Morel and Lebreton 2008) to model stellar evolution with accretion. Cesam2k20 is an open-source, one-dimensional stellar evolution code (available at the [Cesam2k20 website](#)) that employs a spectral method to solve the stellar structure equations given in Eqns. (1). To our knowledge, it is the only stellar evolution code that utilizes a spectral method, which offers the advantages of superconvergence and high numerical precision compared to the more commonly used finite-difference methods in stellar evolution modeling. The following subsections describe its numerical implementation, including the choice of variables, automatic grid-point allocation, the formulation of the structure equations, and the adopted input physics.

### 4.2.1 Lagrangian variables

The system of equations in Eqns. (1) encapsulates the fundamental physics governing stellar structure and evolution. However, in numerical implementation, these equations are often reformulated to improve stability and convergence. One effective approach, discussed by Morel (1997), is to use the set of variables introduced by Eggleton (1971),

$$\left(\frac{m}{M_\odot}\right)^{2/3}, \quad \left(\frac{r}{R_\odot}\right)^2, \quad \left(\frac{l}{L_\odot}\right)^{2/3}, \quad l \geq 0$$

This choice improves numerical precision and helps avoid singularities at the stellar center. In cases where  $l < 0$ —which can occur during late evolutionary stages—the variable  $l/L_\odot$  is used instead. Since this project focuses on the pre-main sequence phase, where such cases do not arise, we adopt the Eggleton variables throughout.

Additionally, because pressure and temperature can span several orders of magnitude in the stellar interior, it is numerically advantageous to work with their logarithms. Accordingly, the set of variables ultimately used in Cesam2k20 is:

$$\xi = \ln P, \quad \eta = \ln T, \quad \zeta = \left(\frac{r}{R_\odot}\right)^2, \quad \lambda = \left(\frac{l}{L_\odot}\right)^{2/3}, \quad \mu = \left(\frac{m}{M_\odot}\right)^{2/3}. \quad (9)$$

### 4.2.2 Automatic location of grid points

To resolve the large variations in physical quantities during stellar evolution, an adaptive grid is necessary. To achieve automatic allocation, Cesam2k20 uses a strictly monotonic spacing function,  $Q(\mu, t)$ , to distribute grid points based on local physical conditions. Grid points are placed such that the difference in  $Q(\mu, t)$  between adjacent points is equal to a time-dependent spacing function  $\psi(t)$  (Eggleton 1971; Morel 1997; Press et al. 1992).

Formally, at each time step  $t$ , the grid points  $\mu_i$ ,  $i = 1, \dots, n$  are allocated such that:

$$Q(\mu_{i+1}, t) - Q(\mu_i, t) = \psi(t), \quad i = 1, \dots, n-1, \quad (10)$$



where  $\psi(t)$  is determined during the numerical integration.

The default form of the spacing function  $Q(\mu, t)$  used in Cesam2k20 is:

$$Q(\mu, t) = (-1)\xi + (0)\eta + (0)\zeta + (0)\lambda + (15)\mu, \quad (11)$$

where the values in parentheses serve as weights for each variable in the calculation of the distance between grid points. See Manchon (2021) and Morel (1997) for the rationale behind this choice. These coefficients can be adjusted in the numerical settings to achieve higher resolution in specific variables if desired. The dependence of  $Q(\mu, t)$  on pressure ( $\xi$ ) and mass ( $\mu$ ) ensures finer resolution in regions of steep pressure and density gradients. In the core, where the pressure gradient is modest, resolution is primarily controlled by mass change; while in the outer envelope, where pressure varies rapidly, the grid is refined mostly based on pressure changes.

To map physical coordinates onto the numerical grid, Cesam2k20 defines an index function  $q(\mu, t)$  that takes integer values from 1 to  $n$  at the grid points. Values of physical variables at positions between grid points are obtained by interpolation on the grid. The derivative of  $Q$  with respect to this index gives:

$$\left. \frac{\partial Q}{\partial q} \right|_t = \left. \frac{\partial Q}{\partial \mu} \right|_t \left. \frac{\partial \mu}{\partial q} \right|_t = \theta(\mu, t) \left. \frac{\partial \mu}{\partial q} \right|_t = \psi(t), \quad (12)$$

where  $\theta(\mu, t)$  is directly obtained from the analytic form of  $Q(\mu, t)$  in Eq. (11).

The introduction of  $\psi(t)$  and  $\theta(\mu, t)$  requires two additional equations for closure:

$$\frac{\partial \mu}{\partial q} = \frac{\psi}{\theta}, \quad \frac{\partial \psi}{\partial q} = 0. \quad (13)$$

The first equation relates the mass coordinate to grid index, while the second enforces constant spacing in  $Q$ -space. This approach enables efficient resolution of the stellar structure, especially during rapid evolutionary phases.

### 4.2.3 Structure equations

With the variables introduced in Secs. 4.2.1 and 4.2.2, the stellar structure equations can be expressed in a form more suitable for integration on an equidistant grid in the numerical index  $q_i = 1, \dots, n$ .

The full set of structure and composition equations solved at each time step is:

$$0 = \frac{\partial \xi}{\partial q} - \left[ -\frac{3G}{8\pi} \left( \frac{M_\odot}{R_\odot} \right)^2 \left( \frac{\mu}{\zeta} \right)^2 + \frac{M_\odot}{4\pi R_\odot} \left( \frac{\mu}{\zeta} \right)^{1/2} \Omega^2 \right] e^{-\xi} \frac{\psi}{\theta}, \quad (14a)$$

$$0 = \frac{\partial \eta}{\partial q} - \left[ -\frac{3G}{8\pi} \left( \frac{M_\odot}{R_\odot} \right)^2 \left( \frac{\mu}{\zeta} \right)^2 + \frac{M_\odot}{4\pi R_\odot} \left( \frac{\mu}{\zeta} \right)^{1/2} \Omega^2 \right] e^{-\xi} \frac{\psi}{\theta} \nabla, \quad (14b)$$

$$0 = \frac{\partial \zeta}{\partial q} - \frac{3}{4\pi} \frac{M_\odot}{R_\odot^3} \frac{1}{\rho} \left( \frac{\mu}{\zeta} \right)^{1/2} \frac{\psi}{\theta}, \quad (14c)$$

$$0 = \frac{\partial \lambda}{\partial q} - \frac{M_\odot}{L_\odot} \left( \frac{\mu}{\lambda} \right)^{1/2} (\epsilon + \epsilon_\nu + \epsilon_g) \frac{\psi}{\theta}, \quad (14d)$$

$$0 = \frac{\partial \mu}{\partial q} - \frac{\psi}{\theta}, \quad (14e)$$

$$0 = \frac{\partial \psi}{\partial q}, \quad (14f)$$

$$0 = \frac{\partial X_i}{\partial t} + \frac{2}{3M_\odot \mu^{1/2}} \frac{\partial F_i}{\partial \mu} - \Psi_i(\xi, \eta, \mathbf{X}), 1 \leq i \leq n_{\text{elem}}. \quad (14g)$$

These equations are solved simultaneously with boundary conditions-at the center:

$$\zeta(1, t) = 0, \quad \lambda(1, t) = 0, \quad \mu(1, t) = 0, \quad (15)$$

and at the surface:

$$\xi(n, t) = \xi_{\text{atm}}(L_{\star}, R_{\star}, t), \quad \eta(n, t) = \eta_{\text{atm}}(L_{\star}, R_{\star}, t), \quad \mu(n, t) = \mu_{\text{atm}}, \quad (16)$$

along with constitutive relations (e.g., equations of state, opacity laws) to evolve the stellar model in time.

#### 4.2.4 Input physics

Although Cesam2k20 is capable of modeling rotation and diffusion, I keep the input physics simple at this stage to focus on the impact of accretion on stellar structure. The interactions of accretion with rotation and diffusion will be an important aspect in future work. The models are computed for 1D, single stars without rotation, magnetic fields, or diffusion. Mass loss is not considered; the only mechanism that alters the stellar mass is accretion. The initial chemical composition follows the solar mixture of Asplund et al. (2009), with meteoritic determination for non-volatile elements as recommended by Serenelli et al. (2009), with the exception of the deuterium abundance, which is varied to explore its impact on accreting stars.

Convection is modeled using the mixing-length theory (MLT) (Cox and Giuli 1968). It assumes that convective energy transport occurs via fluid elements moving from hotter to cooler regions over a characteristic distance-the mixing length—typically taken to be proportional to the pressure scale height. This proportionality is set by the mixing-length parameter,  $\alpha_{\text{MLT}}$ . We adopt a solar-calibrated value of  $\alpha_{\text{MLT}} = 1.64$ . Convective boundaries are determined using the Schwarzschild criterion, with no convective overshooting.

The equation of state (EoS) and opacity are interpolated from the OPAL2005 tables (Iglesias and Rogers 1996; Rogers and Nayfonov 2002; Rogers and Iglesias 1992), and supplemented at low temperatures by the AF opacity tables (Ferguson et al. 2005). Nuclear reaction rates are based on NACRE (Aikawa et al. 2006) and LUNA (Broggini et al. 2018) tables. The models include the full PP and CNO cycles, tracking the evolution of abundances for  $^1\text{H}$ ,  $^2\text{H}$ ,  $^3\text{He}$ ,  $^4\text{He}$ ,  $^7\text{Li}$ ,  $^7\text{Be}$ ,  $^{12}\text{C}$ ,  $^{13}\text{C}$ ,  $^{14}\text{N}$ ,  $^{15}\text{N}$ ,  $^{16}\text{O}$ ,  $^{17}\text{O}$ .

Neutrino energy losses are treated using the prescriptions of Haft et al. (1994) for plasma neutrinos and Weigert (1966) for photoneutrinos. The atmosphere is implemented using a Hopf  $T(\tau)$  relation from Hubeny and Mihalas (2015), with the base of the atmosphere set at an optical depth of  $\tau_{\text{max}} = 20$ , where the solution of the internal structure equations is matched to that of the atmosphere model.

The input physics are summarized in Table 1. Building on this framework, I next describe the implementation of accretion in Cesam2k20.

#### 4.2.5 PMS initial models

At time  $t = 0$ , to begin the computation, the values of pressure  $P(m, 0)$ , temperature  $T(m, 0)$ , radius  $R(m, 0)$ , luminosity  $L(m, 0)$ , and chemical abundances  $\mathbf{X}(m, 0)$  must be specified for  $m \in [0, M_{\star}(t = 0)]$ . In Cesam2k20, these values are taken from precomputed tables of a homogeneous PMS stellar model. Cesam2k20 also has the capacity to start from a ZAMS initial model, or continue the evolution of a previous model. However, for the purpose of this project, I need to start from a PMS model, therefore I will not go into the details of these two other methods of initialization.



Parameter Type	Description
Mass	accretion + no mass loss
Chemical composition	AGS09+S10 <sup>1</sup>
Convection	MLT <sup>2</sup> + No overshoot
Diffusion	None
EoS	OPAL2005 <sup>3</sup>
Opacity	OPAL and AF <sup>4</sup>
Nuclear reaction	NACRE + LUNA <sup>5</sup>
Atmosphere	Hopf <sup>6</sup> , $\tau_{\max} = 20.0$

Table 1: Summary of input parameters for Cesam2k20 models; refer to the text for more details.

This initialization method from a PMS model is based on the work of Iben (1965). At the zero-age of the PMS phase, the star’s only energy source is gravitational contraction, with no contribution from nuclear burning or neutrino losses, i.e.,  $\epsilon = 0$  and  $\epsilon_\nu = 0$ . Furthermore, the star is fully convective, so it has a constant entropy profile throughout its interior. In this regime, the energy equation (Eq. (1d)) simplifies to:

$$\frac{\partial l}{\partial m} = \epsilon_g = -T \frac{\partial s}{\partial t} = cT, \quad (17)$$

where  $c$  is a contraction constant, with units of  $L_\odot M_\odot^{-1} \text{K}^{-1}$ , characteristic of a fully convective star in quasi-equilibrium. Varying the value of  $c$  shifts the starting point of the star’s evolution track in the HR diagram.

The Iben method proceeds by constructing two PMS models, labeled #1 and #2, with the same mass  $M_*$ , but slightly different contraction constants  $c_1$  and  $c_2$ . These models should be close enough that the change in gravitational energy between them approximates the radiative energy loss over a time step  $\Delta t$ :

$$\frac{L_1 + L_2}{2} \Delta t \sim \left( \frac{GM^2}{R_2} - \frac{GM^2}{R_1} \right), \quad (18)$$

where  $L_1, R_1$  and  $L_2, R_2$  are the luminosities and radii of models #1 and #2, respectively (cf. Eq. (13) Morel 1997). Evolution can then proceed using model #2 and time step  $\Delta t$ .

In Cesam2k20, the user provides an input value  $c_1 = c$ , the Iben constant, and the code sets  $c_2 = 1.1 c_1$ . The appropriate range of values for  $c$  depends on the stellar mass. At fixed mass, a lower Iben constant leads to lower luminosity and a higher central temperature. For example,  $c = 0.02$  yields  $T_c \sim 10^5 \text{ K}$ , while smaller values such as  $c = 0.005$  and  $c = 0.00008$  correspond to  $T_c \sim 5 \times 10^5 \text{ K}$  and  $10^6 \text{ K}$ , respectively. Although these values are similar in order of magnitude across different stellar masses, each mass range requires its own acceptable interval of  $c$  values to ensure convergence to a valid PMS model.

## 4.3 Accretion in Cesam2k20

### 4.3.1 From Lagrangian to Homologous variables

The difficulty in implementing accretion in Cesam2k20 lies in the fact that properties of the accreted material are not known a priori, so assumptions must be made about the properties to make this information available.

### 4.3.2 Modifications to the structure equations

In Cesam2k20, the solution of the non-linear boundary problem is done by Newton-Raphson iterations, or known as the Henyey method (Henyey et al. 1959) in context of stellar evolution (Henyey et al. 1955). The structure equations are solved iteratively, with the Jacobian matrix of the system of equations being updated at each iteration. The Jacobian matrix contains the partial derivatives of the structure equations with respect to the variables, which are used to guide the convergence of the solution.

My main modification to the structure equations is in the energy equation, i.e., Eq.(14d), and then of course, the relevant partial derivatives in the Jacobian matrix.

### 4.3.3 Limiting the maximum change in gravitational energy

### 4.3.4 Limiting the maximum change in mass

## 5 Results

### 5.1 The toy problem

- the toy problem of static models, without accretion but differ slightly in mass to emulate the effect of accretion
- one with full convective stars and the other with radiative core
- ? the profile of the gravitational energy and the heat from accretion
- show the problem with this kind of approach necessitate the implementation of accretion in the actual evolution
- can also show the entropy profile inside to star to illustrate the problem of discontinuity

### 5.2 The effect of different initial models

### 5.3 The effect of different accretion rates

### 5.4 The effect of different chemical compositions

- compare accreting models with and without deuterium accreted in the outer layers
- can try to vary the abundance of deuterium in the accreted material

### 5.5 Comparison with Palla & Stahler (1993)

- try to reproduce a similar plot of Palla & Stahler (1992) mass-radius relation, or Fig 20.3 in Maeder book

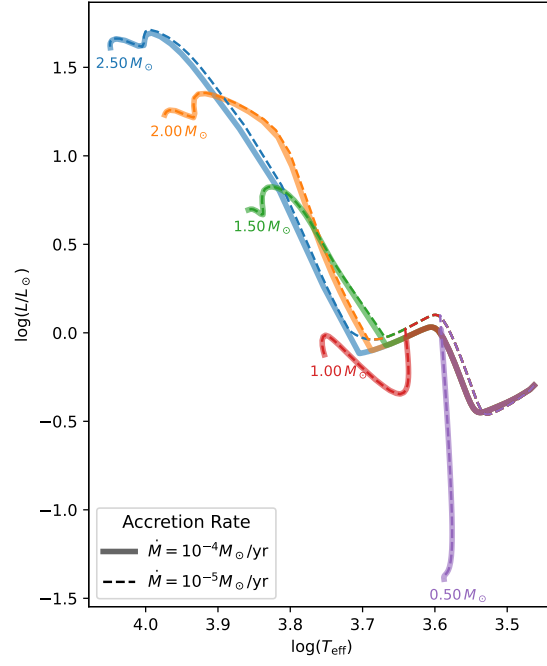


Figure 4: Comparisons of low-mass accreting models with accretion rates of  $10^{-5} M_{\odot}/\text{yr}$  (wide, solid lines) and  $10^{-4} M_{\odot}/\text{yr}$  (thin, dashed lines). The models are initialized with a seed mass of  $0.1 M_{\odot}$  and a deuterium abundance of  $D/H = 2.0 \times 10^{-5}$ .

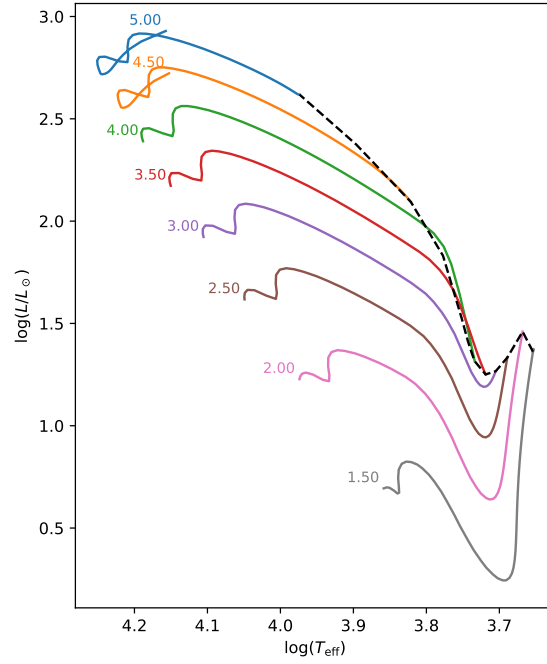


Figure 5: Birthline of accreting stars, with an accretion rate of  $10^{-5} M_{\odot}/\text{yr}$ .

## 6 Conclusion

- summarize the main findings of the project
- discuss the limitations and prospects of this research
- limitations of the current implementation
  - the seed mass is  $0.1M_{\odot}$  can be smaller
  - angular momentum is not considered
  - variable accretion rate
  - numerical treatment of convective-radiative boundary
  - hot/cold accretion

## References

- Aikawa, M. et al. (2006). “NACRE Update and Extension Project”. In: *Frontiers in Nuclear Structure, Astrophysics, and Reactions*. Vol. 831. AIP, pp. 26–30. DOI: [10.1063/1.2200894](https://doi.org/10.1063/1.2200894).
- Alencar, S. H. P. et al. (2012). “Accretion Dynamics in the Classical T Tauri Star V2129 Ophiuchi”. In: *Astronomy and Astrophysics* 541, A116. DOI: [10.1051/0004-6361/201118395](https://doi.org/10.1051/0004-6361/201118395).
- Asplund, M. et al. (2009). “The Chemical Composition of the Sun”. In: *Annual Review of Astronomy and Astrophysics* 47 (Volume 47, 2009), pp. 481–522. DOI: [10.1146/annurev.astro.46.060407.145222](https://doi.org/10.1146/annurev.astro.46.060407.145222).
- Bally, J. (2016). “Protostellar Outflows”. In: *Annual Review of Astronomy and Astrophysics* 54, pp. 491–528. DOI: [10.1146/annurev-astro-081915-023341](https://doi.org/10.1146/annurev-astro-081915-023341).
- Baraffe, I., G. Chabrier, and J. Gallardo (2009). “Episodic Accretion at Early Stages of Evolution of Low-Mass Stars and Brown Dwarfs: A Solution for the Observed Luminosity Spread in H-R Diagrams?” In: *The Astrophysical Journal* 702, pp. L27–L31. DOI: [10.1088/0004-637X/702/1/L27](https://doi.org/10.1088/0004-637X/702/1/L27).
- Baraffe, I., E. Vorobyov, and G. Chabrier (2012). “Observed Luminosity Spread in Young Clusters and FU Ori Stars: A Unified Picture”. In: *The Astrophysical Journal* 756, p. 118. DOI: [10.1088/0004-637X/756/2/118](https://doi.org/10.1088/0004-637X/756/2/118).
- Bouvier, J. (2014). “The Magnetospheric Accretion/Ejection Process in Young Stellar Objects: Open Issues and Perspectives”. In: *European Physical Journal Web of Conferences*. Vol. 64. eprint: arXiv:1310.4439, p. 09001. DOI: [10.1051/epjconf/20136409001](https://doi.org/10.1051/epjconf/20136409001).
- Bouvier, J. et al. (2007). *Magnetospheric Accretion in Classical T Tauri Stars*. DOI: [10.48550/arXiv.astro-ph/0603498](https://doi.org/10.48550/arXiv.astro-ph/0603498). URL: <https://ui.adsabs.harvard.edu/abs/2007prpl.conf..479B>. Pre-published.
- Broggini, C. et al. (2018). “LUNA: Status and Prospects”. In: *Progress in Particle and Nuclear Physics* 98, pp. 55–84. DOI: [10.1016/j.pnpnp.2017.09.002](https://doi.org/10.1016/j.pnpnp.2017.09.002).
- Cox, J. P. and R. T. Giuli (1968). *Principles of Stellar Structure*.
- Eggleton, P. P. (1971). “The Evolution of Low Mass Stars”. In: *Monthly Notices of the Royal Astronomical Society* 151, p. 351. DOI: [10.1093/mnras/151.3.351](https://doi.org/10.1093/mnras/151.3.351).
- Ferguson, J. W. et al. (2005). “Low-Temperature Opacities”. In: *The Astrophysical Journal* 623, pp. 585–596. DOI: [10.1086/428642](https://doi.org/10.1086/428642).
- Gorti, U. and D. Hollenbach (2009). “Photoevaporation of Circumstellar Disks By Far-Ultraviolet, Extreme-Ultraviolet and X-Ray Radiation from the Central Star”. In: *The Astrophysical Journal* 690, pp. 1539–1552. DOI: [10.1088/0004-637X/690/2/1539](https://doi.org/10.1088/0004-637X/690/2/1539).
- Grevesse, N. and A. J. Sauval (1998). “Standard Solar Composition”. In: *Space Science Reviews* 85, pp. 161–174. DOI: [10.1023/A:1005161325181](https://doi.org/10.1023/A:1005161325181).
- Guillot, T. and P. Morel (1995). “CEPAM: A Code for Modeling the Interiors of Giant Planets.” In: *Astronomy and Astrophysics Supplement Series* 109, pp. 109–123.
- Haft, M., G. Raffelt, and A. Weiss (1994). “Standard and Nonstandard Plasma Neutrino Emission Revisited”. In: *The Astrophysical Journal* 425, p. 222. DOI: [10.1086/173978](https://doi.org/10.1086/173978).
- Hartmann, L., G. Herczeg, and N. Calvet (2016). “Accretion onto Pre-Main-Sequence Stars”. In: *Annual Review of Astronomy and Astrophysics* 54 (Volume 54, 2016), pp. 135–180. DOI: [10.1146/annurev-astro-081915-023347](https://doi.org/10.1146/annurev-astro-081915-023347).
- Hartmann, L. et al. (1998). “Accretion and the Evolution of T Tauri Disks”. In: *The Astrophysical Journal* 495, pp. 385–400. DOI: [10.1086/305277](https://doi.org/10.1086/305277).

- Hayashi, C. (1961). “Stellar Evolution in Early Phases of Gravitational Contraction.” In: *Publications of the Astronomical Society of Japan* 13, pp. 450–452.
- Heney, L. G., R. Lelevier, and R. D. Levée (1955). “The Early Phases of Stellar Evolution”. In: *Publications of the Astronomical Society of the Pacific* 67, p. 154. DOI: [10.1086/126791](https://doi.org/10.1086/126791).
- Heney, L. G. et al. (1959). “A Method for Automatic Computation of Stellar Evolution.” In: *The Astrophysical Journal* 129, p. 628. DOI: [10.1086/146661](https://doi.org/10.1086/146661).
- Herbst, W. et al. (2007). *The Rotation of Young Low-Mass Stars and Brown Dwarfs*. DOI: [10.48550/arXiv.astro-ph/0603673](https://doi.org/10.48550/arXiv.astro-ph/0603673). URL: <https://ui.adsabs.harvard.edu/abs/2007prpl.conf..297H> (visited on 06/10/2025). Pre-published.
- Hosokawa, T., S. S. R. Offner, and M. R. Krumholz (2011). “On the Reliability of Stellar Ages and Age Spreads Inferred from Pre-main-sequence Evolutionary Models”. In: *The Astrophysical Journal* 738, p. 140. DOI: [10.1088/0004-637X/738/2/140](https://doi.org/10.1088/0004-637X/738/2/140).
- Hubeny, I. and D. Mihalas (2015). *Theory of Stellar Atmospheres. An Introduction to Astrophysical Non-equilibrium Quantitative Spectroscopic Analysis*.
- Iben Jr., I. (1965). “Stellar Evolution. I. The Approach to the Main Sequence.” In: *The Astrophysical Journal* 141, p. 993. DOI: [10.1086/148193](https://doi.org/10.1086/148193).
- Iglesias, C. A. and F. J. Rogers (1996). “Updated Opal Opacities”. In: *The Astrophysical Journal* 464, p. 943. DOI: [10.1086/177381](https://doi.org/10.1086/177381).
- Ireland, L. G. et al. (2020). “Magnetic Braking of Accreting T Tauri Stars: Effects of Mass Accretion Rate, Rotation, and Dipolar Field Strength”. In: *The Astrophysical Journal* 906.1, p. 4. DOI: [10.3847/1538-4357/abc828](https://doi.org/10.3847/1538-4357/abc828).
- Kastner, J. H. et al. (2002). “Evidence for Accretion: High-Resolution X-Ray Spectroscopy of the Classical T Tauri Star TW Hydrae”. In: *The Astrophysical Journal* 567, pp. 434–440. DOI: [10.1086/338419](https://doi.org/10.1086/338419).
- Kippenhahn, R., A. Weigert, and A. Weiss (2013). *Stellar Structure and Evolution*. DOI: [10.1007/978-3-642-30304-3](https://doi.org/10.1007/978-3-642-30304-3).
- Koenigl, A. (1991). “Disk Accretion onto Magnetic T Tauri Stars”. In: *The Astrophysical Journal* 370, p. L39. DOI: [10.1086/185972](https://doi.org/10.1086/185972).
- Kunitomo, M. and T. Guillot (2021). “Imprint of Planet Formation in the Deep Interior of the Sun”. In: *Astronomy & Astrophysics* 655, A51. DOI: [10.1051/0004-6361/202141256](https://doi.org/10.1051/0004-6361/202141256).
- Kunitomo, M. et al. (2017). “Revisiting the Pre-Main-Sequence Evolution of Stars - I. Importance of Accretion Efficiency and Deuterium Abundance”. In: *Astronomy & Astrophysics* 599, A49. DOI: [10.1051/0004-6361/201628260](https://doi.org/10.1051/0004-6361/201628260).
- Lanzafame, A. C. et al. (2023). “Gaia Data Release 3. Stellar Chromospheric Activity and Mass Accretion from Ca II IRT Observed by the Radial Velocity Spectrometer”. In: *Astronomy and Astrophysics* 674, A30. DOI: [10.1051/0004-6361/202244156](https://doi.org/10.1051/0004-6361/202244156).
- Larson, R. B. (1969). “Numerical Calculations of the Dynamics of Collapsing Proto-Star”. In: *Monthly Notices of the Royal Astronomical Society* 145, p. 271. DOI: [10.1093/mnras/145.3.271](https://doi.org/10.1093/mnras/145.3.271).
- Lii, P. S. et al. (2014). “Propeller-Driven Outflows from an MRI Disc”. In: *Monthly Notices of the Royal Astronomical Society* 441.1, pp. 86–100. DOI: [10.1093/mnras/stu495](https://doi.org/10.1093/mnras/stu495).
- Manara, C. F. et al. (2017). “X-Shooter Study of Accretion in Chamaeleon I. II. A Steeper Increase of Accretion with Stellar Mass for Very Low-Mass Stars?” In: *Astronomy and Astrophysics* 604, A127. DOI: [10.1051/0004-6361/201630147](https://doi.org/10.1051/0004-6361/201630147).
- Manchon, L. (2021). “On the Transport of Angular Momentum in Stellar Radiative Zones in 2D”. PhD thesis. Université Paris-Saclay.

- Marques, J. P. et al. (2013). “Seismic Diagnostics for Transport of Angular Momentum in Stars. I. Rotational Splittings from the Pre-Main Sequence to the Red-Giant Branch”. In: *Astronomy and Astrophysics* 549, A74. DOI: [10.1051/0004-6361/201220211](https://doi.org/10.1051/0004-6361/201220211).
- Morel, P. (1997). “CESAM: A Code for Stellar Evolution Calculations”. In: *Astronomy and Astrophysics Supplement Series* 124, pp. 597–614. DOI: [10.1051/aas:1997209](https://doi.org/10.1051/aas:1997209).
- Morel, P. and Y. Lebreton (2008). “CESAM: A Free Code for Stellar Evolution Calculations”. In: *Astrophysics and Space Science* 316, pp. 61–73. DOI: [10.1007/s10509-007-9663-9](https://doi.org/10.1007/s10509-007-9663-9).
- Muzerolle, J., N. Calvet, and L. Hartmann (2001). “Emission-Line Diagnostics of T Tauri Magnetospheric Accretion. II. Improved Model Tests and Insights into Accretion Physics”. In: *The Astrophysical Journal* 550, pp. 944–961. DOI: [10.1086/319779](https://doi.org/10.1086/319779).
- Muzerolle, J. et al. (2003). “Accretion in Young Stellar/Substellar Objects”. In: *The Astrophysical Journal* 592, pp. 266–281. DOI: [10.1086/375704](https://doi.org/10.1086/375704).
- Palla, F. and S. W. Stahler (1993). “The Pre-Main-Sequence Evolution of Intermediate-Mass Stars”. In: *The Astrophysical Journal* 418, p. 414. DOI: [10.1086/173402](https://doi.org/10.1086/173402).
- Press, W. H. et al. (1992). *Numerical Recipes in FORTRAN. The Art of Scientific Computing*.
- Rogers, F. J. and A. Nayfonov (2002). “Updated and Expanded OPAL Equation-of-State Tables: Implications for Helioseismology”. In: *The Astrophysical Journal* 576, pp. 1064–1074. DOI: [10.1086/341894](https://doi.org/10.1086/341894).
- Rogers, F. J. and C. A. Iglesias (1992). “Rosseland Mean Opacities for Variable Compositions”. In: *The Astrophysical Journal* 401, p. 361. DOI: [10.1086/172066](https://doi.org/10.1086/172066).
- Romanova, M. M. et al. (2004). “The Propeller Regime of Disk Accretion to a Rapidly Rotating Magnetized Star”. In: *The Astrophysical Journal* 616.2, p. L151. DOI: [10.1086/426586](https://doi.org/10.1086/426586).
- Rugel, M., D. Fedelev, and G. Herczeg (2018). “X-Shooter Observations of Low-Mass Stars in the  $\eta$  Chamaeleontis Association”. In: *Astronomy and Astrophysics* 609, A70. DOI: [10.1051/0004-6361/201630111](https://doi.org/10.1051/0004-6361/201630111).
- Serenelli, A. M. et al. (2009). “NEW SOLAR COMPOSITION: THE PROBLEM WITH SOLAR MODELS REVISITED”. In: *The Astrophysical Journal* 705.2, p. L123. DOI: [10.1088/0004-637X/705/2/L123](https://doi.org/10.1088/0004-637X/705/2/L123).
- Stahler, S. W. (1983). “The Birthline for Low-Mass Stars.” In: *The Astrophysical Journal* 274, pp. 822–829. DOI: [10.1086/161495](https://doi.org/10.1086/161495).
- Stahler, S. W. and F. Palla (2004). *The Formation of Stars*.
- Stelzer, B. and R. Neuhauser (2001). “X-Ray Emission from Young Stars in Taurus-Auriga-Perseus: Luminosity Functions and the Rotation - Activity - Age - Relation”. In: *Astronomy and Astrophysics* 377, pp. 538–556. DOI: [10.1051/0004-6361:20011093](https://doi.org/10.1051/0004-6361:20011093).
- Weigert, A. (1966). “Sternentwicklung VI: Entwicklung Mit Neutrinoverlust Und Thermische Pulse Der Helium-Schalenquelle Bei Einem Stern von 5 Sonnenmassen”. In: *Zeitschrift für Astrophysik* 64, p. 395.

## **A Appendix: The jacobian of the stellar structure equations**